Generalized Linear Periodic Time-Varying Analysis for Noise Reduction in an Active Mixer

Jongrit Lerdworatawee, *Member, IEEE*, and Won Namgoong

***Abstract*—A simple linear periodic time-varying circuit model is proposed to rigorously analyze the noise behavior in an active mixer. This analysis can be shown to be a generalization of existing LPTV mixer models, which assume that the mixer is a memoryless device and, as a result, is valid for low frequency only. Based on the proposed LPTV circuit model, explicit formulas for noise figure that accounts for the effect of the thermal noise folding and the flicker noise leakage are derived. Our analysis shows that the mixer operating at OFF overlap mode yields a better noise performance. The analysis is validated against simulations and measurements.**

***Index Terms*—CMOS analog integrated circuit, integrated circuit noise, mixer noise, nonlinear circuit, time-varying circuits.**

I. Introduction

DIRECT CONVERSION receivers (DCRs) have recently attracted widespread attention as they enable high levels of integration and potentially low power consumption [1], [2]. In DCR, the received RF signal is downconverted directly to the baseband for amplification and eventual digitization. One of the main challenges of implementing a DCR is that low-frequency noise such as flicker noise can dominate the signal strength and, if not removed, substantially degrades the signal-to-noise ratio (SNR) [3], [4]. Since the flicker noise arises predominately from the mixer, the design of a good mixer is of significant importance in improving the performance of the DCR.

The two commonly used mixers are active and passive mixers [5]. The active mixer is attractive in many applications because it provides higher conversion gain, resulting in improved suppression of noise contribution from subsequent stages [7]–[8]. Hence, we consider active mixers only, although the proposed analysis approach is also applicable to passive mixers.

To mitigate the flicker noise at the mixer output, the two common approaches are to reduce the current passing through the transistor and to increase the transistor size. Both approaches, however, are at the expense of reduced conversion gain and/or mixer bandwidth. An approach that has not been previously studied for active mixers is to modify the switching mode of the mixer. Depending on the bias voltage at the switched transistor pair, the switching mode can be classified as operating either in the OFF or ON overlap mode [9], [10]. Although originally defined for passive mixers, the OFF and ON overlap modes of operation can also be similarly defined for active mixers as described in the following section. Conventional mixers operate in the ON overlap mode. The use of OFF overlap mode has been studied for passive mixers and shown to suffer from poor noise performance [9], [10]. In active mixers, however, we show that the OFF overlap mode is very effective at reducing the mixer output noise [11].

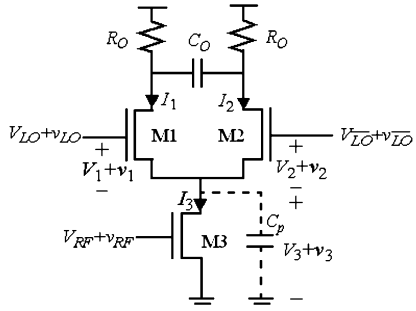

Fig. 1. Single-balance active CMOS mixer.

To accurately predict the mixer noise when operating in both ON and OFF overlap modes, a novel analytical approach to rigorously analyze the mixer noise performance is developed. In the proposed approach, the mixer is modeled as a linear periodic time-varying (LPTV) system [12]–[14]. The proposed analysis approach can be shown to be a generalization of [15] and [16], which assume that the mixers are memoryless devices and, as a result, is valid for low frequency only. In this paper, explicit formulas for the mixer output noise statistic are derived. A noise performance comparison between mixers operating in the ON and OFF overlap modes is carried out in a rigorous manner. The analysis is validated by simulation and experimental measurement results.

The paper is organized as follows. In Section II, we present a new analysis for the active mixer which is modeled as an LPTV system. In Section III, the noise analysis is presented. In Section IV, simulation results are presented to verify the theory, followed by the experimental results in Section V. Conclusions are drawn in Section VI.

II. Mixer Switching Modes

Fig. 1 shows a single-balanced CMOS active mixer, which consists of an input transconductance device (M3), the switched differential pairs (M1 and M2) which are assumed to be symmetric, and the load network which forms a low-pass *RC* filter to the output. In Fig. 1, the voltage $V_{\rm RF}$ biases M3 at the current I_3 to enable voltage-to-current conversion of the input RF signal voltage to the signal current. The resulting input RF signal

Manuscript received November 21, 2005; revised February 1, 2007. This work was supported in part by the National Science Foundation (ECS-0501619) and the Army Research Office (DAAD19-01-1-0477).

J. Lerdworatawee is with Silicon Laboratories, Austin, TX 78701 USA (e-mail: jongrit@hotmail.com).

W. Namgoong is with Atheros Communications, Santa Clara, CA 95054 USA (e-mail: wnamgoong@yahoo.com).

Digital Object Identifier 10.1109/JSSC.2007.896519

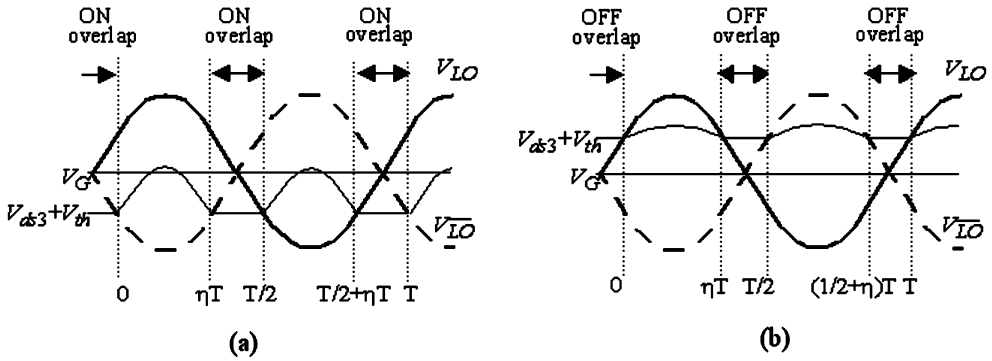

Fig. 2. ON and OFF overlap operation mode.

current is then downconverted by switches M1 and M2 to the output differential current I_O $(=I_1-I_2)$. Note that M1 and M2 are driven by a local oscillator (LO) signal voltage, which alternatively turns on M1 and M2. When either M1 or M2 turns on, it is assumed that it remains in saturation. Keeping M1 and M2 in saturation ensures a higher output resistance, better isolation between the input and output ports, and improved linearity.

The LO switching operation can be classified as operating in either ON or OFF overlap mode. Fig. 2 illustrates two anti-phase sinusoidal voltage signals $V_{\rm LO}$ and $V_{\overline{\rm LO}}$. Here $V_{\rm LO}=V_G+A_{\rm LO}\sin\omega_{\rm LO}t$ and $V_{\overline{\rm LO}}=V_G-A_{\rm LO}\sin\omega_{\rm LO}t$, where $\omega_{\rm LO}$ is the angular LO frequency, V_G is the common voltage and $A_{\rm LO}$ is the LO amplitude. Depending on the relative value of V_G to the M3 drain-source voltage $(V_{\rm ds3})$ and the device threshold voltage $(V_{\rm th})$, the active mixer operates in either ON or OFF overlap mode. Here the overlap refers to a window in transition time where the switched differential pairs are in the same state, i.e., both M1 and M2 are on (or off) during the ON (or OFF) overlap. As shown in the top of Fig. 2, the ON overlap mode occurs when $V_G>V_{\rm ds3}+V_{\rm th}$, whereas the OFF overlap occurs when $V_G<V_{\rm ds3}+V_{\rm th}$. As a result, the ON (or OFF) overlap respectively correspond to the time interval Δ when $V_{\rm LO}$ and $V_{\overline{\rm LO}}$ are greater (or less) than $V_{\rm ds3}+V_{\rm th}$, i.e., $[\eta{\rm T},{\rm T}/2]$ and $[{\rm T}/2+\eta{\rm T},{\rm T}]$ as illustrated in Fig. 2. Here $\Delta=(1/2-\eta)\,T$ and η can be computed by

$$\eta=\frac{1}{2}-\frac{1}{\pi}\arcsin\left(\left|\frac{V_G-V_{\rm th}-V_{\rm ds3,edge}}{A_{\rm LO}}\right|\right) \qquad (1)$$

where $V_{\rm ds3,edge}$ is the value of $V_{\rm ds3}$ at the beginning of the ON (or OFF) overlap period. Note that the polarity of $(V_G-V_{\rm th}-V_{\rm ds3,edge})$ is positive (or negative) for ON (or OFF) overlap while its absolute value is actually determined by the size ratio of M1 (or M2) to M3 and the current during the non-overlap period. For a fixed size ratio and the current, $A_{\rm LO}$ modulates the ON (or OFF) overlap time interval through η, which now becomes a function of $A_{\rm LO}$ for a given bias voltage V_G according to (1). As the LO amplitude increases, η gradually increases and eventually approaches 1/2.

During the ON (or OFF) overlap, the switches M1 and M2 are on (or off) as shown in Fig. 2. When outside the ON (or OFF) overlap interval, one of them (i.e., M1 or M2) remains in saturation while the other is completely off. To effectively downconvert the input signal, M3 is assumed to be in saturation for both ON and OFF overlap mode when outside of the ON (or OFF) overlap interval. On the other hand, M3 remains in saturation during the ON overlap; whereas it gradually switches from saturation to triode mode during the OFF overlap. As M3 acts as a resistor in the latter case, it discharges the capacitor at the drain of M3 to ground, resulting in a voltage drop in $V_{\rm ds3}$. If the OFF overlap time is sufficiently long, $V_{\rm ds3}$ will eventually reduce to zero. These assumptions are made throughout this paper.

The conventional active mixer operates in the ON overlap mode. A potential drawback of operating in this mode is that the low frequency noise (e.g., the flicker noise) generated by switches M1 and M2 can readily leak to the output during the ON overlap interval. This noise is referred to as the direct noise in [15]. To reduce the direct noise, larger LO amplitude with sharper LO transition can be applied. However, even in the extreme case when LO is a square waveform with infinite slope, flicker noise still appears because of the charging and discharging of the capacitance at the tail node. This noise is referred to as the indirect noise in [15].

To reduce the flicker noise, we propose to operate in the OFF overlap mode. In principle, this method can eliminate the direct noise since it prevents both switches from turning on simultaneously. On the other hand, the mixers when operating in the OFF overlap mode can be shown to have less indirect noise leakage to the output. This is because the amount of the charging and discharging noise current is reduced as portion of the voltage noise stored at the tail node has been leaked through M3 to ground during the OFF overlap. As a result, the indirect noise can be minimized by properly adjusting the OFF overlap interval as described in a later section. A potential drawback when operating in the OFF overlap mode is that the mixer suffers from lower conversion gain. Since less power is dissipated in this mixer, however, the loss in conversion gain becomes negligible when the two mixers are compared under equal power dissipation condition.

III. Modeling the Mixer as a Linear Periodic Time-Varying System

In the proposed analysis, the mixer is modeled as an LPTV system, which can be characterized by a transfer function that is periodically time-varying [17]. Unlike in previous LPTV mixer model [16], which assumes a memoryless device, our analysis accounts for the memory effect of the tail capacitor. For clarity of discussion, the review of the fundamental theory for the LPTV system is summarized in the Appendix. In this

section, we make use of the results from the theory to derive the closed-form LPTV transfer functions, which are used to compute parameters such as conversion gain and noise figure in the following section.

A. Characterizing the Active Mixer

The mixer in Fig. 1 can be described by the following set of nonlinear differential equations:

$$\begin{aligned} I_1(V_1) + I_2(V_2) &= I_3(V_3, V_{\rm RF}) + \frac{d}{dt}Q_C(V_3) \\ V_1 - V_2 &= V_{\rm LO} - V_{\overline{\rm LO}} \\ V_3 + \frac{V_1 + V_2}{2} &= \frac{V_{\rm LO} + V_{\overline{\rm LO}}}{2} \\ I_O &= I_1(V_1) - I_2(V_2) \end{aligned} \tag{2}$$

where I_X and V_X (for $X = 1, 2$, and 3) are the current and voltage as shown in Fig. 1. In addition, Q_C is the charge stored in the capacitance at the drain node of M3. This capacitance consists of the gate-source capacitance of M1 and M2 (i.e., $C_{\rm gs1}$ and $C_{\rm gs2}$) and the junction capacitances at the source of M1 and M2 and the drain of M3. Since they appear as a nonlinear function of the applied voltage, these junction capacitances make the underlying linear assumption for the time-varying model invalid and therefore make the analysis too complicated. To overcome this difficulty, we approximate these junction capacitances as a time-invariant capacitance $C_{\rm eff}$. This $C_{\rm eff}$ can be theoretically computed as a time-average of these capacitances. As a result, the total capacitance at the tail node is the sum of $C_{\rm gs1}, C_{\rm gs2}$ and $C_{\rm eff}$ and is defined as a time-invariant C_p illustrated by the dash line in Fig. 1.

As a first step to determining the LPTV transfer function, we linearize (2) around a time-varying operating point, resulting in the following linearized small-signal differential equation:

$$\begin{aligned} \frac{\partial}{\partial t}(\boldsymbol{C}v(t)) + \boldsymbol{G}(t)\boldsymbol{v}(t) &= \boldsymbol{B}(t)\boldsymbol{w}(t) \\ i_Q(t) &= \boldsymbol{D}(t)\boldsymbol{v}(t). \end{aligned} \tag{3}$$

As illustrated in Fig. 1, $i_O\ (t)$ is the small-signal differential output current, $\boldsymbol{w}(t)\ (= [v_{\rm RF}(t), v_{\rm LO}(t), v_{\overline{\rm LO}}(t)]^T)$ is the small-signal input vector, and $\boldsymbol{v}(t)\ (= [v_1(t), v_2(t), v_3(t)]^T)$ is the small-signal state vector. The time-invariant capacitance matrix $\boldsymbol{C}$ and time-varying (trans)conductance matrix $\boldsymbol{G}(t)$, $\boldsymbol{D}(t)$, and $\boldsymbol{B}(t)$ are given by

$$\boldsymbol{C} = \begin{bmatrix} 0 & 0 & -C_p \\ 0 & 0 & 0 \\ 0 & 0 & 0 \end{bmatrix} \tag{4}$$

$$\boldsymbol{D}(t) = \begin{bmatrix} g_{m1}(t) & -g_{m2}(t) & 0 \end{bmatrix} \tag{5}$$

$$\boldsymbol{G}(t) = \begin{bmatrix} g_{m1}(t) & g_{m2}(t) & -g_{\rm ds3}(t) \\ 1 & -1 & 0 \\ 1/2 & 1/2 & 1 \end{bmatrix} \tag{6}$$

$$\boldsymbol{B}(t) = \begin{bmatrix} g_{m3}(t) & 0 & 0 \\ 0 & 1 & -1 \\ 0 & 1/2 & 1/2 \end{bmatrix}. \tag{7}$$

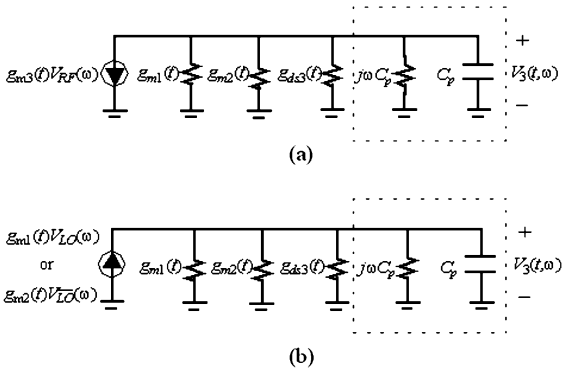

Fig. 3. PSSC model.

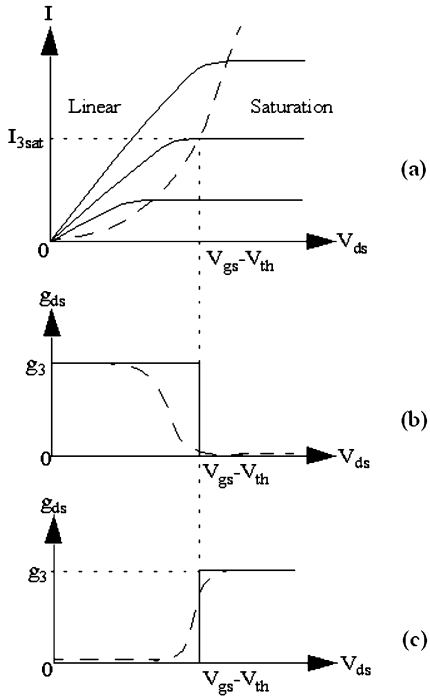

Fig. 4. I-V curve for MOS transistors and the corresponding g_m and $g_{\rm ds}$.

B. Periodic Steady-State Circuit Model

To perform the periodic steady-state analysis for an LPTV system, we assume that the inputs are sinusoidal signals with time-invariant amplitude, i.e., $v_{\rm RF}(t) = V_{\rm RF}(\omega)\exp(j\omega t)$, $v_{\rm LO}(t) = V_{\rm LO}(\omega)\exp(j\omega t)$ and $v_{\overline{\rm LO}}(t) = V_{\overline{\rm LO}}(\omega)\exp(j\omega t)$. The state voltage and output current are sinusoidal signals with periodic time-varying amplitude, i.e., $v_X(t) = V_X(t,\omega)\exp(j\omega t)$ and $i_O(t) = I_O(t,\omega)\exp(j\omega t)$, where $\boldsymbol{V}_X(t,\omega) = \boldsymbol{V}_X(t+T,\omega)$ and $\boldsymbol{I}_O(t,\omega) = \boldsymbol{I}_O(t+T,\omega)$. Substituting them in (2), we obtain a new equation for the time-varying amplitude of the state voltage and the output current at frequency ω, i.e., [19]

$$\begin{aligned} \left[\boldsymbol{C}\frac{\partial}{\partial t} + \boldsymbol{G}_{\rm eff}(t,\omega)\right]\boldsymbol{V}(t,\omega) &= \boldsymbol{B}(t)\boldsymbol{W}(\omega) \\ I_O(t,\omega) &= \boldsymbol{D}(t)\boldsymbol{V}(t.\omega) \end{aligned} \tag{8}$$

where $\boldsymbol{V}(t,\omega) = [V_1(t,\omega), V_2(t,\omega)V_3(t,\omega)]^{\rm T}$, $\boldsymbol{W}(\omega) = [V_{\rm RF}(\omega), V_{\rm LO}(\omega), V_{\overline{\rm LO}}(\omega)]^{\rm T}$, and $\boldsymbol{G}_{\rm eff}(t,\omega) = \boldsymbol{G}(t) + j\omega\boldsymbol{C}$.

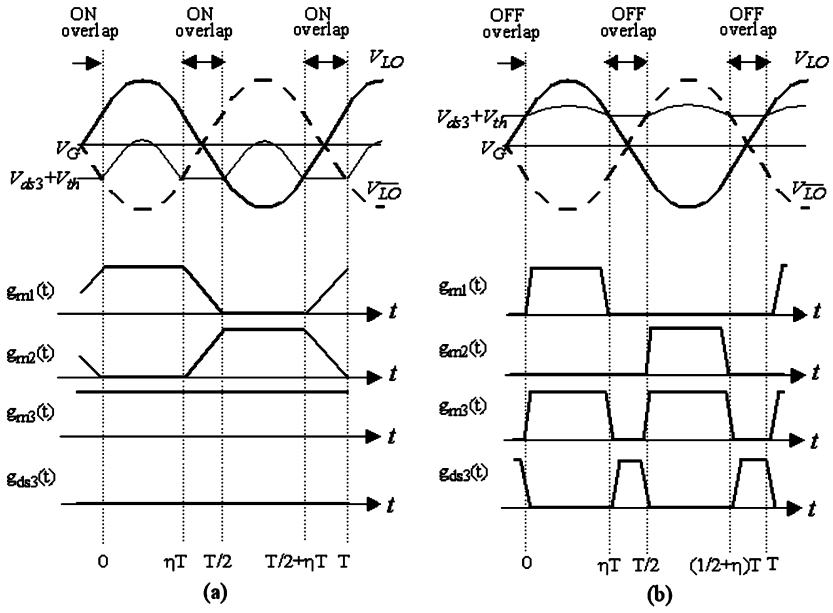

Fig. 5. Linear piecewise approximation for g_m (t) and $g_{\rm ds}$ (t).

Note that if the capacitive effect is neglected, the terms in the bracket at the left-hand side of (8) reduces to $\boldsymbol{G}(t)$. The resulting memoryless LPTV equations, which are valid at low frequencies, have been solved in [16].

Since the elements in the second and third rows of $\boldsymbol{C}$ (see (4)) are all zero, the state vector computation is greatly simplified. Substituting (4)- (7) into (8), it can be shown that for input $V_{\rm RF}(\omega)$, $V_1(t,\omega) = V_2(t,\omega) = -V_3(t,\omega)$. Similarly, input $V_{\rm LO}(\omega)$ yields $V_1(t,\omega) = V_{\rm LO}(\omega) - V_3(t,\omega)$ and $V_2(t,\omega) = -V_3(t,\omega)$; while input $V_{\overline{\rm LO}}(\omega)$ results in $V_1(t,\omega) = -V_3(t,\omega)$ and $V_2(t,\omega) = V_{\overline{\rm LO}}(\omega) - V_3(t,\omega)$. As $V_1(t,\omega)$ and $V_2(t,\omega)$ can be deduced from $V_3(t,\omega)$, only the knowledge of $V_3(t,\omega)$ is required.

To better understand how $V_3(t,\omega)$ is affected by inputs $V_{\rm RF}(\omega)$ and $V_{\rm LO}(\omega)$ (or $V_{\overline{\rm LO}}(\omega)$), we introduce an equivalent circuit model of (8) as shown in Fig. 3. This circuit model of the amplitude response at frequency ω is subsequently referred to as the periodic steady-state circuit (PSSC) model. In this model, the gate of M1, M2 and M3 are connected to an analog ground according to (8). This model includes a resistor with imaginary value of $j\omega C_p$ and a capacitor of C_p (as illustrated by the dash-line block) to account for the tail capacitance. If this capacitive effect is neglected (i.e., $C_p = 0$), the PSSC model becomes memoryless and valid at low frequency only. To accurately predict the behavior of the mixer at all frequencies, the proposed PSSC model shown in Fig. 3 is solved for $V_3(t,\omega)$ as described in the following subsection.

After solving for $V_3(t,\omega)$, the contributions of $V_{\rm RF}(\omega)$, $V_{\rm LO}(\omega)$, and $V_{\overline{\rm LO}}(\omega)$ to the differential output current $I_O(t,\omega)$ can be readily obtained:

$$\begin{aligned} I_O(t,\omega) &= -\left[g_{m1}(t) - g_{m2}(t)\right] V_3(t,\omega) \\ &= P(t,\omega) V_{\rm RF}(\omega) \end{aligned} \tag{9}$$

$$\begin{aligned} I_O(t,\omega) &= g_{m1}(t) V_{\rm LO}(\omega) - \left[g_{m1}(t) - g_{m2}(t)\right] V_3(t,\omega) \\ &= M(t,\omega) V_{\rm LO}(\omega) \end{aligned} \tag{10}$$

$$\begin{aligned} I_O(t,\omega) &= -g_{m2}(t) V_{\overline{\rm LO}}(\omega) - \left[g_{m1}(t) - g_{m2}(t)\right] V_3(t,\omega) \\ &= Q(t,\omega) V_{\overline{\rm LO}}(\omega). \end{aligned} \tag{11}$$

Since M1 and M2 are assumed symmetric, $g_{m2}(t) = g_{m1}(t - T/2)$. As a result, when $V_{\rm LO}(t,\omega) g_{m1}(t)$ or $V_{\overline{\rm LO}}(t,\omega)\, g_{m2}(t)$ is applied as shown in Fig. 3, $V_3(t,\omega)$ differs in the two cases simply by a shift of T/2. Using this relationship in (10) and (11), it can be shown that $Q(t,\omega) = -M(t - T/2, \omega)$. Therefore, we consider only $P(t,\omega)$ and $M(t,\omega)$ which are used to distinguish the transfer function from the input RF and LO port to the output IF port.

C. Derivation of $P(t,\omega)$ and $M(t,\omega)$

To derive the LPTV transfer functions $P(t,\omega)$ and $M(t,\omega)$, we first solve for $V_3(t,\omega)$ given inputs $V_{\rm RF}(\omega)$ and $V_{\rm LO}(\omega)$ using the PSSC model in Fig. 3. To determine $V_3(t,\omega)$, we consider the short channel model to describe the current and voltage of a MOS transistor [18], i.e.,

$$I = \begin{cases} \mu_n C_{\rm ox} \left(\dfrac{W}{L}\right) \dfrac{(V_{\rm gs} - V_{\rm th} - V_{\rm ds}/2) V_{\rm ds}}{1 + \theta V_{\rm ds}}, & V_{\rm ds} < V_{\rm gs} - V_{\rm th} \\ \dfrac{\mu_n C_{\rm ox}}{2} \left(\dfrac{W}{L}\right) \dfrac{(V_{\rm gs} - V_{\rm th})^2}{1 + \theta (V_{\rm gs} - V_{\rm th})}, & V_{\rm ds} \geqslant V_{\rm gs} - V_{\rm th} \end{cases} \tag{12}$$

where I is the drain current, $V_{\rm gs}$ is the gate-source voltage, $V_{\rm ds}$ is the drain-source voltage and $V_{\rm th}$ is the threshold voltage of the device. In (12), μ_n is the electron mobility, $C_{\rm ox}$ is the gate oxide capacitance per unit area and the parameter θ models to first order the source series resistance, mobility degradation due to the vertical field, and velocity saturation due to the lateral field.

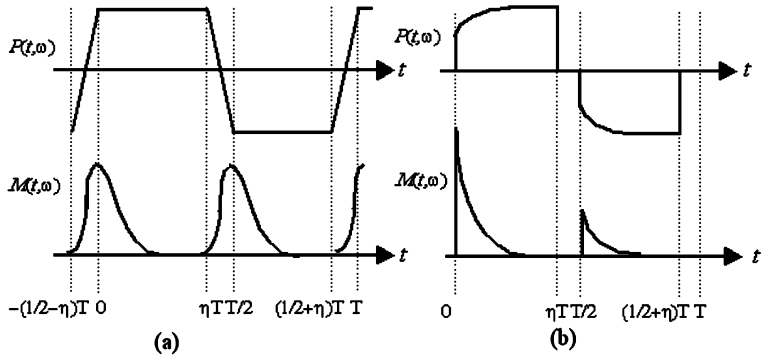

Fig. 6. Plot of $P(t,\omega)$ and $M(t,\omega)$ for (a) ON and (b) OFF overlap mode.

According to (12), Fig. 4(a) plots the current-voltage curves, where the linear and saturation region are separated by a dashed line. Using (12), the PSSC model is difficult to analyze since the transconductance and the drain conductance, i.e., g_m and $g_{\rm ds}$, are a nonlinear function of $V_{\rm ds}$, as illustrated by the dashed line in Fig. 4(b) and (c). To simplify the analysis, we approximate g_m and $g_{\rm ds}$ by a step function as illustrated by the solid line in Fig. 4(b) and (c). As a result, the time-varying g_m and $g_{\rm ds}$ of $\rm M_X$, i.e., $g_{\rm mX}(t)$ and $g_{\rm dsX}(t)$, become a piecewise linear function as illustrated in Fig. 5. Mathematically, they can be given by

$$g_{\rm mX}(t) = \left.\frac{\partial I_X}{\partial V_{\rm gsX}}\right|_{V_{\rm gsX}} \approx \begin{cases} g_X & V_{\rm dsX}(t) > V_{\rm gsX}(t) - V_{\rm th} \\ 0 & V_{\rm dsX}(t) \leqslant V_{\rm gsX}(t) - V_{\rm th} \end{cases} \tag{13}$$

$$g_{\rm dsX}(t) = \left.\frac{\partial I_X}{\partial V_{\rm dsX}}\right|_{V_{\rm dsX}=0} \approx \begin{cases} 0 & V_{\rm dsX}(t) > V_{\rm gsX}(t) - V_{\rm th} \\ g_X & V_{\rm dsX}(t) \leqslant V_{\rm gsX}(t) - V_{\rm th} \end{cases} \tag{14}$$

where, according to (12),

$$g_X = \left(\frac{I_{3\rm sat}}{\theta}\right)\left[1+\sqrt{1+2\mu_n C_{\rm ox}\left(\frac{W}{L}\right)_X\left(\frac{\theta^2}{I_{3\rm sat}}\right)}\right] \tag{15}$$

is determined by the ratio of the transistor width to length and $I_{3\rm sat}$, which is a constant that represents the saturation current of M3 during the non-overlap time interval. Using this approximation, the PSSC model can then be readily solved for $V_3(t,\omega)$ in each linear time segment. The voltage at the boundary of these linear time segments can be made continuous by appropriately solving for the initial conditions of the circuit.

Using the PSSC model with the piecewise linear approximation in Fig. 5 and after some straightforward but tedious algebraic manipulations, $P(t,\omega)$ and $M(t,\omega)$ for both the ON and OFF overlap modes can be readily determined. An example is shown in Fig. 6, which plots $P(t,\omega)$ and $M(t,\omega)$ for both ON and OFF overlap modes assuming ω is near DC. For both overlap modes, $P(t,\omega)$ is an odd periodic function with T (i.e., $P(t,\omega) = -P(t-T/2,\omega)$) and $M(t,\omega)$ is a periodic function with T.

The resulting mathematical expressions for $P(t,\omega)$ and $M(t,\omega)$ are summarized as follows. For the ON overlap mode, we obtain (16) and (17), shown at the bottom of the page, where $\tau_1 = C_p/g_1, \xi_1 \exp(-\Delta/\tau_1)$ and

$$F(\omega) = \frac{g_1}{g_1 + j\omega C_p}. \tag{18}$$

For the OFF overlap mode, we obtain (19) and (20), shown at the bottom of the next page, where $\overline{F(\omega)} = 1 - F(\omega); \tau_2 = C_p/g_3$ and $\xi_2 = \exp(-\Delta/\tau_2)$. As η (or Δ) increases (or decreases), ξ_1 and ξ_2 approach to 1. For $\eta = 1/2$ (or $\Delta = 0$), we can show that (16) and (17) are equal to (19) and (20), respectively, suggesting that the ON and OFF overlap mode become identical as the ON or OFF overlap time disappears.

$$P(t,\omega) = \begin{cases} g_3 F(\omega) & 0 \leqslant t < \eta T \\ g_3 F(\omega)\left[1 - \frac{2(t-\eta T)}{\Delta}\right] & \eta T \leqslant t < T/2 \end{cases} \tag{16}$$

$$M(t,\omega) = \begin{cases} g_1\left\{1 - \left[1 - \frac{\tau_1}{\Delta}(1-\xi_1)e^{\frac{-t}{\tau_1}}\right]F(\omega)\right\} & 0 \leqslant t < \eta T \\ g_1\left\{1 - \frac{t-\eta T}{\Delta} + \left[1 - 2\left(1 - \frac{t-\eta T}{\Delta}\right)\right]\left[1 - \frac{t-\eta T}{\Delta} + \frac{\tau_1}{\Delta}(1 - e^{-\frac{t-\eta T}{\tau_1}})\right]F(\omega)\right\} & \eta T \leqslant t < \frac{T}{2} \\ g_1 F(\omega)\frac{\tau_1}{\Delta}(1-\xi_1)e^{-\frac{t-T/2}{\tau_1}} & \frac{T}{2} \leqslant t < \left(\eta + \frac{1}{2}\right)T \\ g_1\left\{\frac{t-(\eta+1/2)T}{\Delta} - \left(1 - \frac{2[t-(\eta+1/2)T]}{\Delta}\right)\left[\frac{t-(\eta+1/2)T}{\Delta} - \frac{\tau_1}{\Delta}\left(1 - e^{-\frac{t-(\eta+1/2)T}{\tau_1}}\right)\right]F(\omega)\right\} & \left(\eta + \frac{1}{2}\right)T \leqslant t < T \end{cases} \tag{17}$$

IV. Mixer Noise Analysis

Using the expressions for $P(t,\omega)$ and $M(t,\omega)$ derived earlier, the PSD of the mixer output noise is first derived. The noise figure (NF) is then determined.

A. Mixer Output Noise PSD

When the mixer is modeled as an LPTV system, the mixer output noise becomes a cyclostationary process even though the input noise is assumed stationary. In addition to complicating the noise analysis of the mixer, the cyclostationary noise could significantly degrade the mixer noise performance if the correlated noise spectra at multiples of $f_{\rm LO}$ are added. To avoid this problem, a low-pass filter with bandwidth less than $f_{\rm LO}$ is added at the mixer output to filter out the high frequency noise spectra. As illustrated in Fig. 1, this low-pass filter is implemented with the load network. As a result, the noise statistic at the output of the mixer is stationary and can be described in terms of the time-average power spectral density (PSD).

According to the LPTV theory, the time-average PSD of $I_O(t,\omega)$ can be written as

$$S_{I_O}(\omega)=\sum_{n=-\infty}^{\infty}\left|P^{(n)}(\omega)\right|^2 S_{V_{\rm RF}}(\omega-n\omega_{\rm LO}) + \left|M^{(n)}(\omega)\right|^2\left[S_{V_{\rm LO}}(\omega-n\omega_{\rm LO})+S_{V_{\overline{\rm LO}}}(\omega-n\omega_{\rm LO})\right] \quad (21)$$

In (21), $S_{V_{\rm LO}}(\omega), S_{V_{\overline{\rm LO}}}(\omega)$ and $S_{V_{\rm RF}}(\omega)$ are the PSD of the input noise at the gate of $\rm M_1$–$\rm M_3$; $P^{(n)}(\omega)$ and $M^{(n)}(\omega)$ are, respectively, the *n*th order harmonic transfer function of $P(t,\omega-n\omega_{\rm LO})$ and $M(t,\omega-n\omega_{\rm LO})$ as given by [20]

$$P^{(n)}(\omega)=\frac{1}{T}\int_0^T P(t,\omega-n\omega_{\rm LO})\exp(-jn\omega_{\rm LO}t)dt \quad (22)$$

$$M^{(n)}(\omega)=\frac{1}{T}\int_0^T M(t,\omega-n\omega_{\rm LO})\exp(-jn\omega_{\rm LO}t)dt. \quad (23)$$

When the memory effect is considered in an LPTV system, $|P^{(n)}(\omega)|$ (or $|M^{(n)}(\omega)|$) is generally not equal to $|P^{(-n)}(\omega)|$ (or $|M^{(-n)}(\omega)|$), which imply that the upconversion and downconversion gains may be different.

For the single-balanced mixer, the input noise sources consist of the resistive noise, e.g., the RF source resistance R_s, the LO source resistance $R_{\rm LO}$ (typically equal to R_s), the polysilicon gate resistance $r_{\rm gX}$ of MX (for X = 1, 2, and 3), and the transistor noise (e.g., the high-frequency thermal noise and low-frequency flicker noise). Since M1 and M2 are assumed symmetric, $P(t,\omega)$ is odd periodic, and as a result, $P^{(n)}(\omega)=0$ when n is an even number, which implies that no flicker noise is leaked from M3 to the mixer output. In addition, the noise statistic in M1 and M2 are the same i.e., $S_{V_{\rm LO}}(\omega)=S_{V_{\overline{\rm LO}}}(\omega)$. As such, we can rewrite (21) as follows:

$$S_{I_O}(\omega)=4kT_K\left(R_S+r_{g3}+\frac{\gamma}{g_3}\right)\overline{\alpha^2(\omega)}+4kT_K \times\left(R_{\rm LO}+2r_{g1}+\frac{2\gamma}{g_1}\right)\overline{\beta^2(\omega)}+\left(\frac{2K_f}{W_1L_1C_{\rm ox}f}\right)\overline{\beta(\omega)}^2. \quad (24)$$

In (24), $k(=\ 1.38\times10^{-23}\ \rm J/K)$ is the Boltzmann's constant and $T_K\ (=\ 290\ \rm K)$ is the ambient temperature; γ and K_f are the thermal and flicker noise coefficients, $\beta(\omega)\ (=|M^{(0)}(\omega)|)$ denote the flicker noise leakage factor of M1 (and M2), and $\overline{\alpha^2(\omega)}\ (=\sum_{n=-\infty}^{\infty}|P^{(n)}(\omega)|^2)$ and $\overline{\beta^2(\omega)}\ (=\sum_{n=-\infty}^{\infty}|M^{(n)}(\omega)|^2)$ are the thermal noise folding factor of M3 and M1 (and M2).

Using the proposed LPTV analysis approach, the mixer output noise can be quantitatively analyzed. In addition, the reduction in the flicker noise when operating the mixer in the OFF overlap mode can be understood from (24). When operating in the OFF overlap mode, the flicker noise leakage by means of the direct noise mechanism [15] is eliminated, while the contribution via the indirect noise mechanism is greatly suppressed. As illustrated in Fig. 6, the disappearance of the direct noise is due to the absence of the ON overlap interval regardless of η; whereas the reduction in the indirect noise occurs since $V_3(t,\omega)$ is mostly discharged to ground through M3, which enters the linear region during the OFF overlap interval. This discharging process reduces the amount of capacitive current that leaks to the output through M2 at the second half LO cycle, resulting in reduced $\overline{\beta(\omega)}$. To quantify the amount

$$P(t,\omega)=\begin{cases} g_3F(\omega)\left\{1-\left[\frac{1-\xi_2}{1-\xi_2\exp\left(-\frac{\eta T}{\tau_1}\right)}\right]e^{-\frac{t}{\tau_1}}\right\}, & 0\leqslant t<\eta T \\ 0, & \eta T\leqslant t<\frac{T}{2}\end{cases} \quad (19)$$

$$M(t,\omega)=\begin{cases} g_1\left\{\overline{F(\omega)}+F(\omega)\left[\frac{1-\xi_2^2\exp\left(-\frac{\eta T}{\tau_1}\right)}{1-\xi_2^2\exp\left(-\frac{2\eta T}{\tau_1}\right)}\right]e^{-\frac{t}{\tau_1}}\right\}, & 0\leqslant t<\eta T \\ 0, & \eta T\leqslant t<\frac{T}{2} \\ g_1F(\omega)\frac{\left[1-\exp\left(-\frac{\eta T}{\tau_1}\right)\right]\xi_2}{1-\xi_2^2\exp\left(-\frac{2\eta T}{\tau_1}\right)}e^{-\frac{t-T/2}{\tau_1}}, & \frac{T}{2}\leqslant t<\left(\eta+\frac{1}{2}\right)T \\ 0, & \left(\eta+\frac{1}{2}\right)T\leqslant t<T\end{cases} \quad (20)$$

of the indirect noise leaked to the output of the mixers, we can compute $\overline{\beta(\omega)}$ by averaging $M(t,\omega)$ as in (20) over T, i.e.,

$$\overline{\beta(\omega)} = \left|\eta g_1 \overline{F(\omega)} + \frac{1+\xi_2}{T} C_p F(\omega)\right| = \frac{C_p}{T}\left|\frac{1+\xi_2+j\eta\omega T}{1+j\omega\tau_1}\right|. \quad (25)$$

As mentioned in the preceding section, the ON and OFF overlap model becomes the same when $\eta = 1/2$ (or $\Delta = 0$). According to (25), $\overline{\beta(\omega)}$ for both modes then approaches to $2C_p/T$ at low frequency. This result is consistent with the prediction using the simple physical model [15], which in turn verifies the validity of our model. As Δ increases, the discharging process during the OFF overlap time interval becomes more effective and, as a result, $\overline{\beta(\omega)}$ is smaller as ξ_2 in (25) decreases. Therefore, the OFF overlap mode outperforms the ON overlap in terms of the flicker noise reduction.

B. Expressing NF

The mixer NF is defined as the ratio of the total output noise power to the fraction of the output noise power contributed by the input noise source. The amount of the total output noise is determined from (24). The fraction of the mixer output noise caused by the input noise is computed by multiplying the input noise with the conversion gain (CG). In general, we consider the input noise as the thermal noise generated by the 50 Ω input source resistor. As a result, the NF can be written as

$$\mathrm{NF} = \frac{\overline{\alpha^2(\omega)}}{c^2(\omega)}\mathrm{NF}_3 + \frac{\overline{\beta^2(\omega)}}{c^2(\omega)}\mathrm{NF}_2 + \frac{\overline{\beta(\omega)}^2}{c^2(\omega)}(\mathrm{NF}_1 - 1) \quad (26)$$

$$\mathrm{NF}_1 = 1 + \frac{K_f}{2kT_K R_S W_1 L_1 C_{\mathrm{ox}} f} \quad (27)$$

$$\mathrm{NF}_2 = 1 + \frac{2r_{g1}}{R_S} + \frac{2\gamma}{g_1 R_S} \quad (28)$$

$$\mathrm{NF}_3 = 1 + \frac{r_{g3}}{R_S} + \frac{\gamma}{g_3 R_S}. \quad (29)$$

In (26), $\overline{\alpha^2(\omega)}, \overline{\beta^2(\omega)}$ and $\overline{\beta(\omega)}^2$ can be determined from (22) and (23) and $c(\omega)$ $(= |P^{(1)}(\omega)|)$ is closely related to CG (i.e., CG is equal to the product of $c(\omega)$ and the output resistance R_O as shown in Fig. 1). According to (16) and (19), we can compute $c(\omega)$ for the ON and OFF overlap mode as

$$c(\omega) = \begin{cases} \left(\frac{2g_3}{\pi}\right)\frac{\sin\left[\pi\left(\frac{1}{2}-\eta\right)\right]}{\pi\left(\frac{1}{2}-\eta\right)} & \text{ON overlap} \\ \left(\frac{g_3}{\pi}\right)\left|e^{-j2\eta\pi} - \frac{1+j\omega_{\mathrm{LO}}\tau_1\xi_2}{1+j\omega_{\mathrm{LO}}\tau_1}\right| & \text{OFF overlap.} \end{cases} \quad (30)$$

For $\eta = 1/2$ (or $\xi_2 = 1$), note from (30) that $c(\omega)$ for both overlap modes approaches to $(2/\pi)g_3$, which agrees with the prediction from the conventional memoryless mixer model [16].

Of our primary interest is the noise contribution in the last term of (26) due to the flicker noise, which typically dominates the other noise sources at baseband frequency. In particular when operating in the OFF overlap mode, we can obtain an analytical expression to compute the noise figure for the mixers by first neglecting the first and second term in (26) and then substituting (25), (27) and (30) into (26), i.e.,

$$\mathrm{NF} \approx \left(\frac{\tau_2}{T}\right)^2 \frac{\pi^2 K_f}{2kT_K R_S W_1 L_1 C_{\mathrm{ox}} f} \times \left|\frac{1+\xi_2+j\omega T}{(1+j\omega\tau_1)\left[e^{-j2\eta\pi} - \frac{1+j\omega_{\mathrm{LO}}\tau_1\xi_2}{1+j\omega_{\mathrm{LO}}\tau_1}\right]}\right|^2. \quad (31)$$

From (31), we can effectively improve NF by reducing η (or increasing Δ). This noise reduction is, however, at the expense of lowering the conversion gain according to (30). Note that the power consumption depends on the average current $I_{\mathrm{ave}} = 2\eta I_{3\mathrm{sat}}$. Since less power is dissipated with decreasing η, the loss in gain may be compensated by allowing for more power. The trade-offs between the design parameters of the mixers will be discussed in depth in the following section.

V. Simulation Results

To validate our analysis, the single-balanced mixer shown in Fig. 1 was simulated with a sinusoidal LO waveform at frequency of 1 GHz and the mixer's output noise was measured at frequency of 10 kHz using the Periodic Steady State (PSS) analysis of the Cadence Spectre-RF simulator. The transistors were designed in the 0.35-μm standard CMOS process with a supply voltage of 2.5 V. During simulation, the CG and NF performance of the mixers with OFF and ON overlap are compared. To compute the CG in simulation, a signal tone is applied at the input RF port. CG can then be computed by dividing the magnitude of the IF frequency component from the FFT of the output signals by the magnitude of the input signal. When simulating the NF, the thermal noise coefficient was assumed to be 2.5, which is commonly used for the short-channel devices [5]; while the flicker noise coefficient was 4.7×10^{-22}, which was obtained experimentally.

The mixer operating in the ON and OFF overlap modes are compared using both simulation and the proposed LPTV analysis. We assume that M1 and M2 are equally sized and the average power dissipation is set at 5 mW. The design parameters are then the sizes of M1 and M3 (as denoted by W_1 and W_3) and η.

For W_3 fixed at 100 μm, the NF and CG become a function of W_1 and η only. Fig. 7 plots the NF against W_1 for η ranging from 0.4 to 0.5. In this figure, the numerical results using the PSS analysis are plotted as illustrated by the symbols (i.e., circles and squares for the ON overlap mode, up-triangle and down-triangle for the OFF overlap mode and plus when $\eta = 0.5$) while the analytical solutions are represented by the dot-line (for the ON overlap mode) and solid-line (for the OFF overlap mode). A close agreement between our analysis and the PSS simulation is observed.

From Fig. 7, the mixer operating in the OFF overlap mode outperforms the mixer in the ON overlap mode. As η increases, the NF for the ON overlap mode improves. In contrast, the NF for the OFF overlap degrades and eventually the NF for both switching modes are the same when $\eta = 50\%$. Although reducing η improves the NF when operating in the OFF overlap mode, the improvement is marginal for η less than 40%.

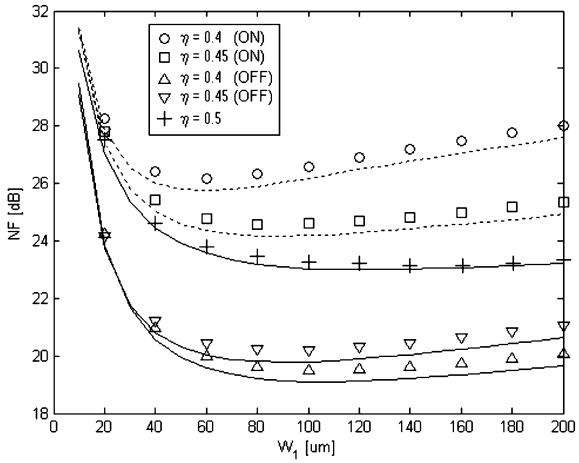

Fig. 7. Noise figure of the ON and OFF overlap modes versus W1 for $W3 = 100$ um and varying η. The dot-line and solid-line respectively represent the analytical results for the ON and OFF overlap mode while the symbols represent numerical results.

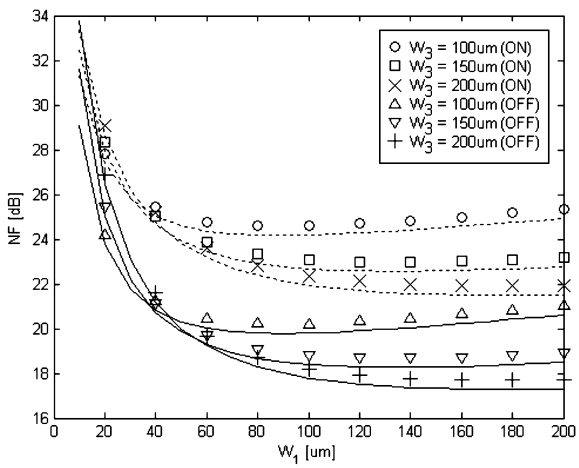

Fig. 8. Noise figure of the ON and OFF overlap modes versus W1 for $\eta = 0.45$ and varying W1. The dot-line and solid-line respectively represent the analytical results for ON and OFF overlap mode while the symbols represent numerical results.

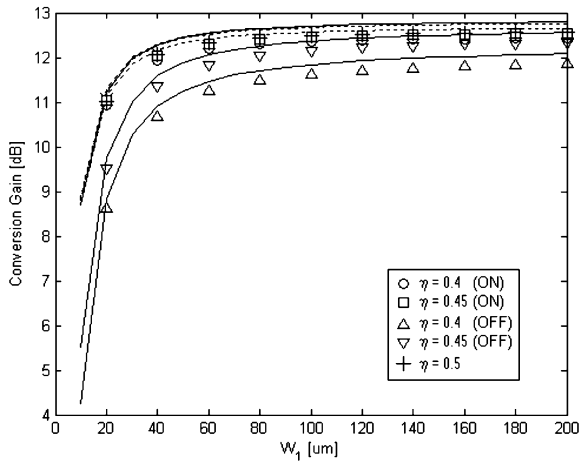

Fig. 9. Conversion gain of the ON and OFF overlap mode versus W1 for $W3 = 100$ um and varying η. The dot-line and solid-line respectively represent the analytical results for ON and OFF overlap mode while the symbols represent numerical results.

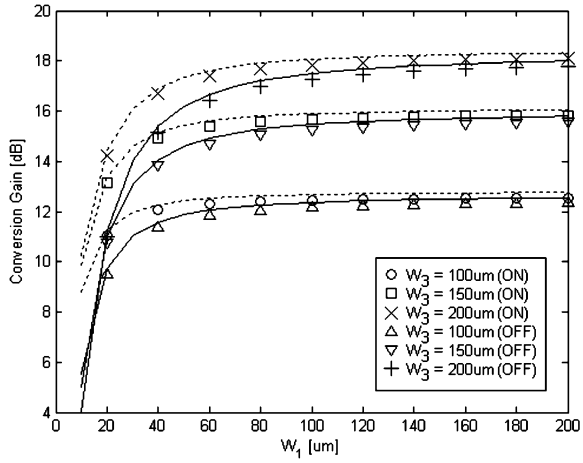

Fig. 10. Conversion gain of the ON and OFF overlap mode versus W1 for $\eta = 0.45$ and varying W3. The dot-line and solid-line respectively represent the analytical results for ON and OFF overlap mode while the symbols represent numerical results.

For a given η, the minimum NF occurs at a particular W_1 regardless of the switching modes. When W_1 is small, the NF is high because the flicker noise introduced by M1 and M2 is large. As W_1 is increased, the NF drops until the gate-source capacitance of M1 and M2 cause C_p to become large, causing the indirect noise to become significant. In the example shown in Fig. 7, the optimum W_1 occurs at 100 um when $\eta = 45\%$ is assumed.

In Fig. 8, NF is plotted against W_1 for W_3 ranging from 100 μm to 200 μm assuming $\eta = 45\%$. By increasing W_3 from 100 μm to 200 μm, the optimum W_1 also increases and the resulting NF is reduced from 20 dB to 17 dB. Although not shown, the NF improvement with increasing W_1 and W_3 is at the expense of reduced mixer bandwidth.

Figs. 9 and 10 plot the CG as a function of W_1 for the same operating conditions as in Figs. 7 and 8, respectively. Compared to the OFF overlap mode, the CG of the ON overlap mode is less sensitive to η. For both switching modes, the CG improves as W_1 and/or W_3 increase but saturates for large W_1 and W_3. Again, this CG improvement is at the expense of reduced mixer bandwidth.

VI. Measurement Results

To validate the mixer concept experimentally, the single-balanced mixer shown in Fig. 1 was fabricated in TSMC 0.35-μm CMOS technology. The switches and the transconductance transistors were equally sized at 200 μm/0.35 μm according to the analysis in the preceding section. The supply voltage is at 2.5 V and the load resistors are 1 kΩ to provide sufficient gain. A block diagram of the test setup is illustrated in Fig. 11. The chip photograph of the mixer core is shown in Fig. 12. As shown in Fig. 11, the gate of the switched transistors and the transconductance transistor were biased at a constant voltage and a sinusoidal LO signal was applied on the switched differential pairs through a balun. To measure the output noise, a low noise current preamplifier was implemented using LT1007. The resulting

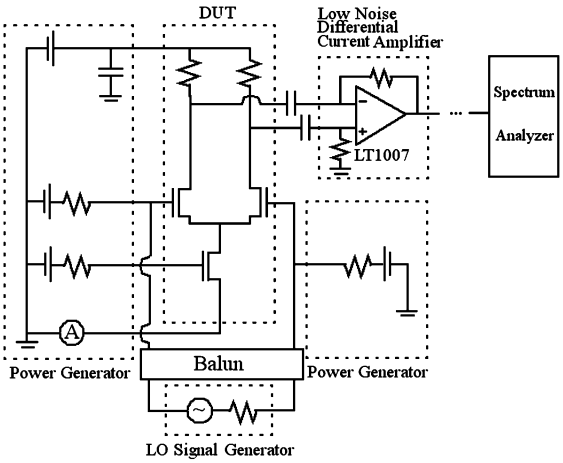

Fig. 11. Diagram for testing.

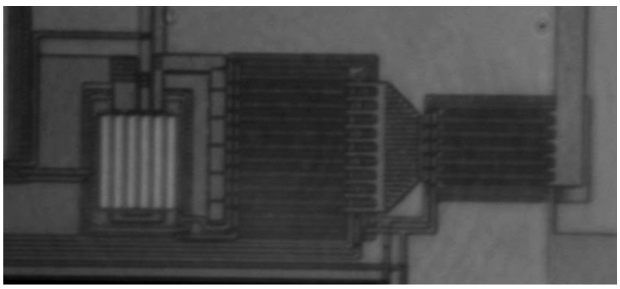

Fig. 12. Chip photograph of the mixer core.

amplified current noise is further amplified then fed to the spectrum analyzer.

As discussed in the preceding section, the optimum η is 50% for the ON overlap mode and 40%–45% for the OFF overlap mode. To allow for the mixer to operate at approximately $\eta = 50\%$ for the ON overlap mode, M1 and M2 bias voltage (i.e., V_G) needs to be greater than $V_{\rm th}$ ($= 0.5$ V) and the LO switching amplitude ($A_{\rm LO}$) must be large, e.g., $V_G = 1$ V and $A_{\rm LO} = 1$ V. In the OFF overlap mode, $V_G = 0$ V and $A_{\rm LO} = 2$ V so that η =42% [according to (1)]. When the LO swings below 0V in the OFF overlap mode, the voltage is clipped by a diode (e.g., ESD).

Fig. 13 presents the measured mixer output current noise PSD between 10 kHz and 500 kHz at two LO frequencies ($f_{\rm LO}$): 1 GHz and 3 GHz. The gate bias of M3 is adjusted so that the average current ($I_{\rm ave}$) is 2 mA (or equivalently 5 mW). For reference, the PSD of the flicker noise measured when the constant bias $V_G = 2$ V is applied to the switches is also included. As shown in Fig. 13, the measured noise is the flicker noise as its spectrum clearly exhibits a $1/f^k$ frequency dependency with the power factor k being very close to unity. Even with the linear piecewise approximation, a close agreement between the measurement results (as illustrated by the symbols) and our analysis using (19) (as illustrated by the dot lines) is observed.

The OFF overlap mode yields a 5 dB reduction in the output noise compared to the ON overlap mode for LO frequency of 1 GHz. This improvement diminishes to approximately 2 dB for LO frequency of 3 GHz. This reduction in the NF gap between the ON and OFF overlap modes occurs with increasing

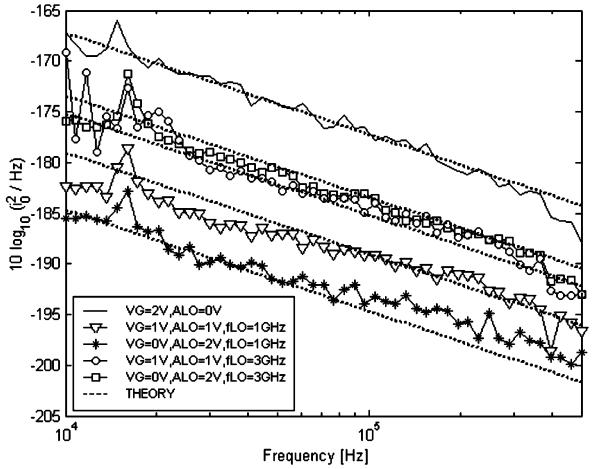

Fig. 13. Measured flicker noise PSD.

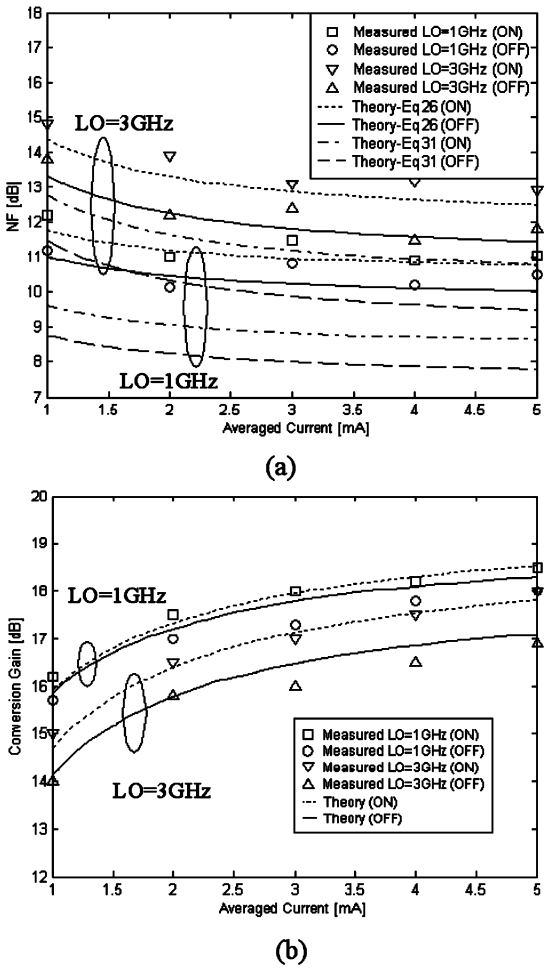

Fig. 14. Measured NF and conversion gain against current at $f_{\rm IF} = 1$ MHz.

frequency because of the difficulty in discharging the tail capacitor. To further validate our model, the performance of the mixer was measured and compared with the simulation results over a wide range of operation points.

With the same V_G and $A_{\rm LO}$ as above, Figs. 14 and 15 present the measured NF and conversion gain of the two mixers against

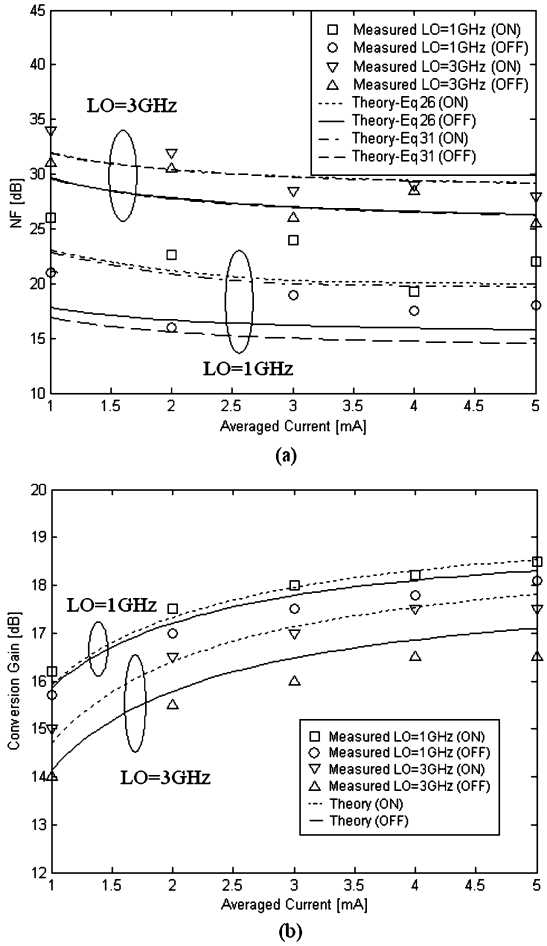

Fig. 15. Measured NF and conversion gain against current at $f_{\rm IF} = 10$ kHz.

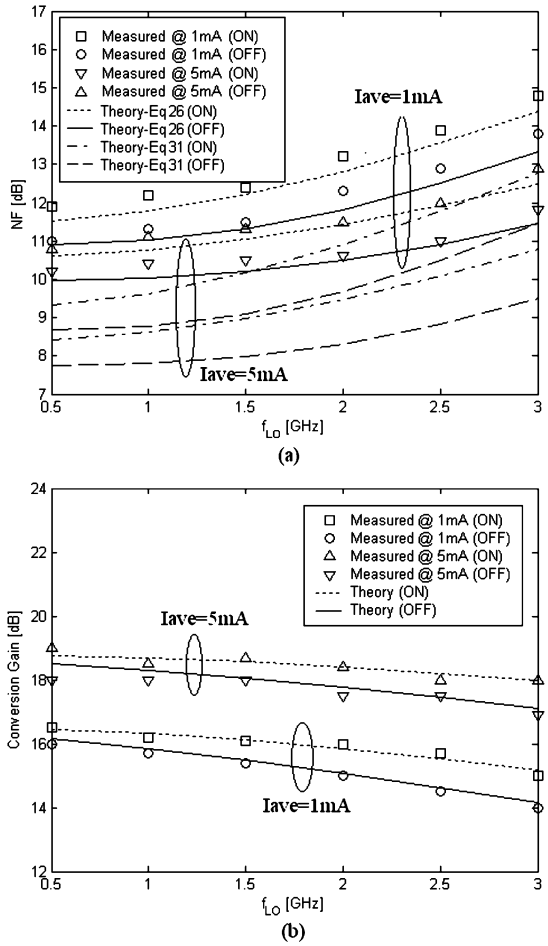

Fig. 16. Measured NF and conversion gain against $f_{\rm LO}$ at $f_{\rm IF} = 1$ MHz.

$I_{\rm ave}$ at different IF frequencies: 1 MHz and 10 kHz. The differences in NF between the ON and OFF overlap mode remain roughly the same regardless of the power dissipated. In contrast, we observe that the loss in conversion gain is negligible when the two mixers are compared under the same power dissipation at low LO frequency, i.e., 1 GHz in this example, which is consistent with the predictions from intuition. However, the loss in conversion gain increases at higher LO frequency. As a result, the advantage of reducing NF in the mixer when operating in the OFF overlap mode may be offset by the loss in gain.

As shown in Figs. 14 and 15, a close agreement between the measurement results and our analysis is observed at different $I_{\rm ave}$. In addition, the measured NF and conversion gain against $f_{\rm LO}$ match well with the predictions from our analysis, as shown in Figs. 16 and 17. Once again, all these results justify the validity of our analysis.

Consider that $I_{\rm ave}$ is 3 mA, which can be achieved by properly adjusting the gate bias voltage of the transconductance transistor, and V_G remains the same as above, i.e., 1 V for the ON and 0 V for the OFF overlap mode. Figs. 18 and 19 present the simulated and measured NF and conversion gain against $A_{\rm LO}$ at two IF frequencies: 1 MHz and 10 kHz. The conversion gain of the mixer operating in the OFF overlap mode is more sensitive to $A_{\rm LO}$ than in the ON overlap mode. This is because, as the LO amplitude increases from $V_{\rm th}$, M3 experiences a transition from linear to saturation during the non-overlap time interval. As a result, g_m of M3 becomes more sensitive to the LO amplitude variation when the LO amplitude is small (or M3 is in linear region) than when the LO amplitude is large (or M3 is in saturation). As the conversion gain is determined by g_m of the transconductance transistor M3, the conversion gain is sensitive to the LO amplitude only when the LO amplitude is close to $V_{\rm th}$.

Based on our analysis, the noise reduction mainly depends on η, which is determined by $A_{\rm LO}$. Before computing η using (1), we obtain $V_{\rm ds3,edge}$ by running the transient analysis in SPICE. Although not explicitly specified, η in Figs. 18 and 19 for the ON overlap mode is approximately equal to 50% when $A_{\rm LO}$ is greater than 0.8 V; whereas for the OFF overlap mode it begins to increase when $A_{\rm LO} = 0.5$ V and eventually approaches to 42% when $A_{\rm LO} = 2$ V. As we reduce the LO amplitudes, the noise figure curves for the two overlap modes actually cross each other. Specifically, compared with the mixer in the ON overlap mode, the mixer noise figure for the OFF overlap mode is higher at small LO amplitudes whereas it is lower at large LO amplitudes. The reason is that at small LO amplitudes the conversion gain for the OFF overlap is low, resulting in increased noise figure. As LO amplitude increases, the conversion gain improves and becomes similar to that for the ON overlap.

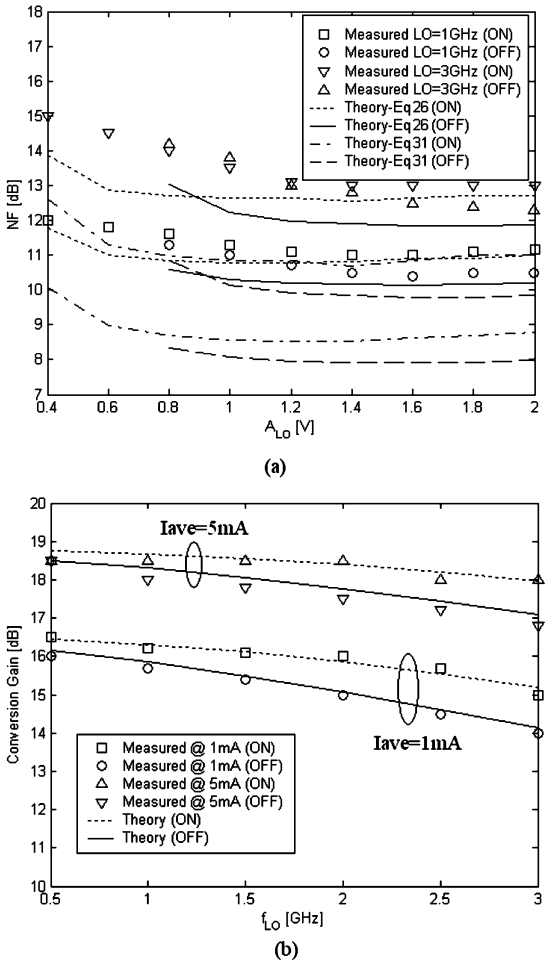

Fig. 17. Measured NF and conversion gain against $f_{\rm LO}$ at $f_{\rm IF} = 10$ kHz.

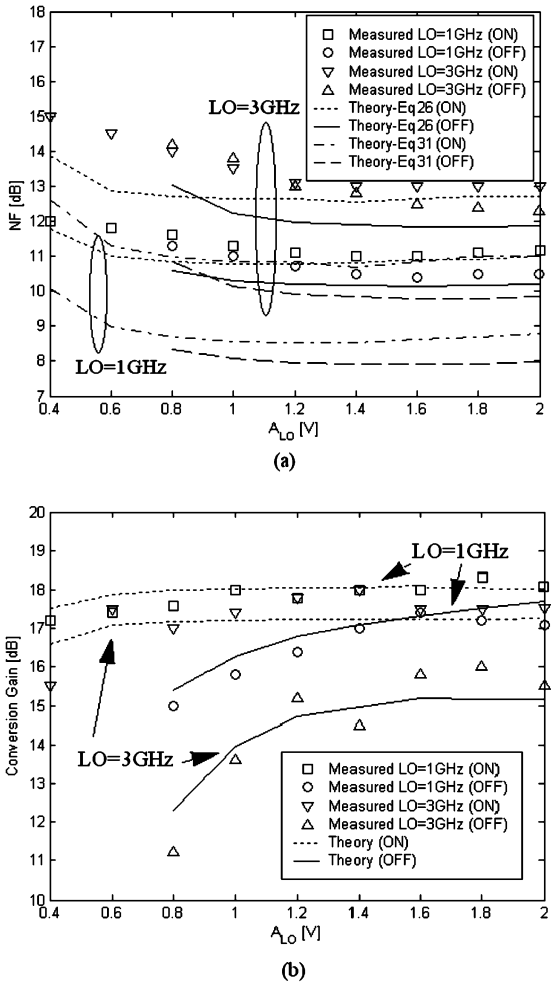

Fig. 18. Measured NF and conversion gain against $A_{\rm LO}$ at $f_{\rm IF} = 1$ MHz.

This increased conversion gain significantly improves the noise figure of the mixer in the OFF overlap mode.

In Figs. 14–19, the theoretical NF predictions using both (26) and (31) are similar at low IF frequency (e.g., 10 kHz). At higher IF frequency (e.g., 1 MHz), the difference increases (by < 3 dB) because the first two terms in (26), which were assumed negligible when obtaining (31), become more significant relative to the third term in (26).

Figs. 20 and 21 show the two linearity metrics of the mixers: IIP2 and IIP3, which are measured and plotted against $I_{\rm ave}$, assuming the LO signal at 1 GHz. For both figures, $V_G = 1$ V and $A_{\rm LO} = 1$ V for the ON overlap mode, and $V_G = 0$ V and $A_{\rm LO} = 2$ V for the OFF overlap mode. Under this assumption, the linearity of the mixers for the ON and OFF overlap modes are compared. Although better IIP3 is observed in the former mixer, it suffers from poorer IIP2 performance compared with the latter mixer. The reasons are as follows. As the transconductance transistor is more linear in the former mixer, less third-order intermodulation product is generated before downconversion to the baseband. On the other hand, less low-frequency second-order intermodulation product is leaked to the output of the latter mixer due to the OFF overlap.

VII. Conclusion

To better analyze the noise performance in a mixer, a simple analytical LPTV circuit model is proposed. This model employs a linear piecewise approximation to describe the periodically time-varying behavior of the small-signal parameters. The proposed analysis can be shown to be a generalization of existing LPTV mixer models, which assumes that the mixer is a memoryless device and, as a result, is valid for low frequency only. Using this model, the thermal noise folding and flicker noise leakage can be better understood. The performance advantage of having the mixer operate in the OFF overlap is demonstrated by simulations, analysis, and experimental measurements.

Appendix

For a general (time-varying) linear system, the relation between the input $x(t)$ and the output $y(t)$ can be given by

$$y(t) = \int h(t,u)x(u)\,du = \frac{1}{2\pi}\int H(t,\varpi)X(\varpi)\exp(j\varpi t)d\varpi \qquad \text{(A1)}$$

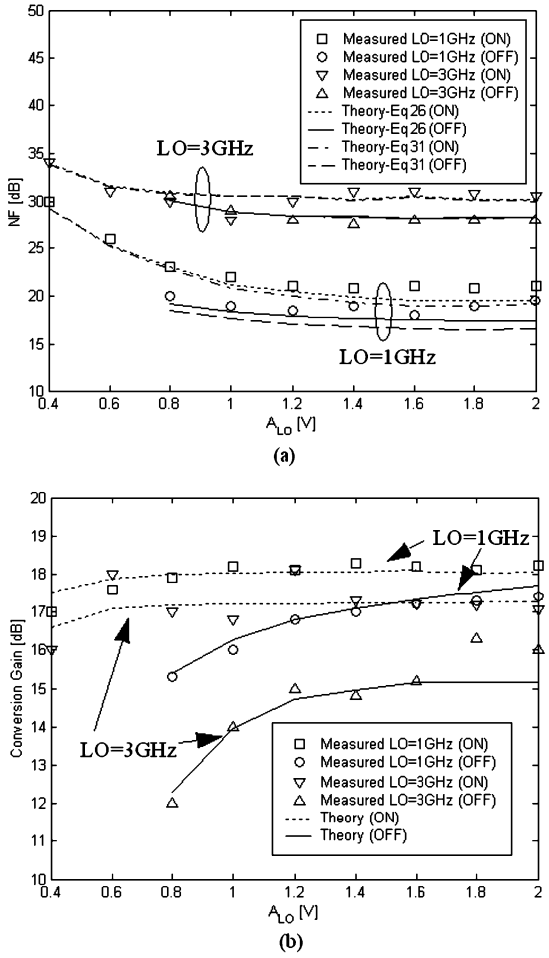

Fig. 19. Measured NF and conversion gain against $A_{\rm LO}$ at $f_{\rm IF} = 10$ kHz.

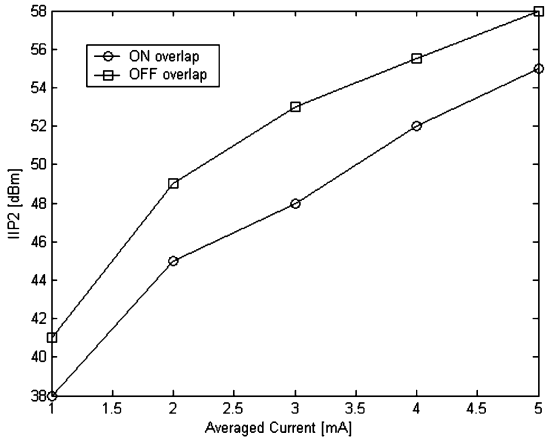

Fig. 20. Measured IIP2 against current at $f_{\rm LO} = 1$ GHz.

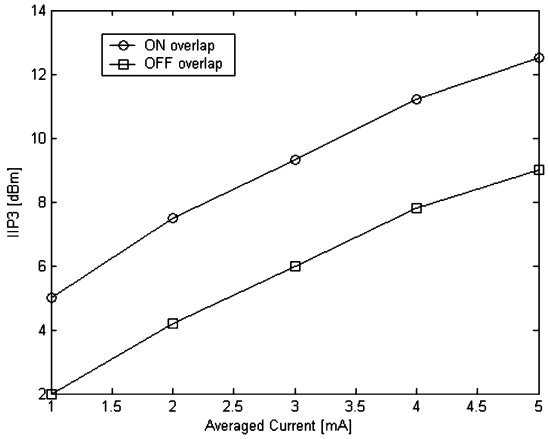

Fig. 21. Measured IIP3 against current at $f_{\rm LO} = 1$ GHz.

where $h(t,u)$ is the impulse response with u denoting the launch time and t denoting the observation time, and $H(t,\varpi)$ is the time-varying transfer function with ϖ denoting the angular frequency corresponding to the delay $v\ (=t-u)$. In (A1), $h(t,u)$ and $H(t,\varpi)$ are a pair of Fourier transform with respect to v, i.e.,

$$\begin{cases} h(t,u) = \frac{1}{2\pi}\int H(t,\varpi)\exp(j\varpi v)dv \\ H(t,\varpi) = \int h(t,u)\exp(-j\varpi v)dv. \end{cases} \tag{A2}$$

The common approach to analyze the mixers driven by the periodic LO signal is to model it as a linear periodic time-varying (LPTV) system. For an LPTV system, $h(t,u)$ and $H(t,\overline{\omega})$ are periodic with respective to T. Therefore, they can be represented by a Fourier series (assumed to converge), i.e.,

$$\begin{cases} h(t,u) = \displaystyle\sum_{n=-\infty}^{\infty} h^{(n)}(v)\exp\left(j\frac{2n\pi}{T}u\right) \\ H(t,\varpi) = \displaystyle\sum_{n=-\infty}^{\infty} H^{(n)}\left(\varpi+\frac{2n\pi}{T}\right)\exp\left(j\frac{2n\pi}{T}t\right) \end{cases} \tag{A3}$$

where $h^{(n)}(v)$ is the harmonic impulse response and $H^{(n)}(\varpi)$ is the harmonic transfer function. Similarly, $h^{(n)}(v)$ and $H^{(n)}(\varpi)$ are another pair of Fourier transform, i.e.,

$$\begin{cases} h^{(n)}(v) = \dfrac{1}{2\pi}\displaystyle\int H^{(n)}(\varpi)\exp j\varpi v d\varpi \\ H(t,\varpi) = \int h^{(n)}(v)\exp -j\varpi v dv. \end{cases} \tag{A4}$$

Substituting (A3) and (A4) into (A1) and taking the Fourier transform to the resulting $y(t)$, we obtain

$$Y(\lambda) = \int y(t)e^{-j\lambda t}\,dt = \sum_n H^{(n)}(\lambda)X\left(\lambda-\frac{2n\pi}{T}\right) \tag{A5}$$

where λ is the angular frequency corresponding to t and $X(\lambda)$ is the Fourier transform of $x(t)$. According to (A5), the frequency translation can be made possible in an LPTV system like the mixers.

Suppose that $x(t)$ is a wide-sense-stationary (WSS) process, $y(t)$ can be shown to a cyclostationary process. Unlike the WSS process, the power spectral densities (PSD) of the cyclostationary process at any two frequencies that are separated by multiples of $1/T$ are correlated. This correlation in different

frequencies is a potential problem in the mixers. To avoid this problem, a filter with bandwidth less than $1/T$ is generally assumed at the output of the mixers. As a result, the mixer output becomes stationary and the resulting correlation function is simply the time average correlation function of $y(t)$ as given by

$$R_y(\tau) = \overline{E\left[y(t+\tau/2)y(t-\tau/2)\right]} = \sum_n \left\{R_X(\tau)e^{-j\frac{2n\pi}{T}}\right\} \otimes r_{nn}(-\tau) \quad \text{(A6)}$$

where τ is the correlation time period and

$$r_{nn}(\tau) = \int h^{(n)}\left(v+\frac{\tau}{2}\right)h^{(n)}\left(v-\frac{\tau}{2}\right)dv \quad \text{(A7)}$$

Note that the bottom of (A6) is obtained by substituting (A1) and (A3) into the top of (A6). By taking the Fourier transform of $R_y(t)$ in (A6), the PSD of $y(t)$ after low-pass filtering can be given by

$$S_y(\omega) = \sum_n \left|H^{(n)}(\omega)\right|^2 S_X\left(\omega - \frac{2n\pi}{T}\right) \quad \text{(A8)}$$

where ω is the angular frequency corresponding to τ and $S_x(\omega)$ is the PSD of $x(t)$. For a memoryless LPTV system, $h(t,u) = h(t)\delta(u)$ and therefore $h^{(n)}(v) = h_n$ and $H^{(n)}(\omega) = H_n$. As a result, $y(t) = h(t)x(t)$ according to (A1) and its PSD reduces to $S_y(\omega) = \sum_n |H_n|^2 S_X(\omega - (2n\pi)/(T))$, according to (A8), which are assumed in the conventional analysis for the mixers.

REFERENCES

[1] A. A. Abidi, "Direct conversion radio transceivers for digital communications," *IEEE J. Solid-State Circuits*, vol. 30, no. 12, pp. 1399–1410, Dec. 1995.

[2] A. Rofougaran, J. Y.-C. Chang, M. Rofougaran, and A. A. Abidi, "A 1 GHz CMOS RF front-end IC for a direct conversion wireless receiver," *IEEE J. Solid-State Circuits*, vol. 31, no. 7, pp. 880–889, Jul. 1995.

[3] B. Razavi, "Design considerations for direct-conversion receivers," *IEEE Trans. Circuits Syst. II*, vol. 44, no. 6, pp. 428–435, Jun. 1997.

[4] D. Manstretta, R. Castello, F. Gatte, P. Rossi, and F. Svelto, "A 0.18-μ m CMOS direct conversion receiver front-end for UMTS," in *IEEE Int. Solid State Circuits Conf. Dig. Tech. Papers*, 2002, pp. 240–241.

[5] T. H. Lee, *The Design of Radio-Frequency Integrated Circuits*. Cambridge: Cambridge Univ., 1998.

[6] J. Crols and M. Steyaert, "A 1.5 GHz highly linear CMOS downconversion mixer," *IEEE J. Solid-State Circuits*, vol. 30, no. 7, pp. 736–742, Jul. 1995.

[7] E. A. M. Klumperink, S. M. Louwsma, G. J. M. Wienk, and B. Nauta, "A CMOS switched transconductor mixer," *IEEE J. Solid-State Circuits*, vol. 39, no. 8, pp. 1231–1240, Aug. 2004.

[8] H. Darabi and J. Chiu, "A noise cancellation technique for active RF-CMOS mixers," *IEEE J. Solid-State Circuits*, vol. 40, no. 12, pp. 2628–2632, Dec. 2005.

[9] D. Ham and A. Hajimiri, "Complete noise analysis for CMOS switching mixers via stochastic differential equations," in *Proc. CICC*, 2000, pp. 439–442.

[10] S. Chehrazi, R. Bagheri, and A. A. Abidi, "Noise in passive FET mixers: A simple physical model," in *Proc. CICC*, 2004, pp. 375–378.

[11] J. Lerdworatawee and W. Namgoong, "Generalized noise analysis of active mixers by simple linear periodic time-varying circuit model," in *Proc. CICC*, 2005, pp. 293–296.

[12] H. D'Angelo, *Linear Time-Varying Systems: Analysis and Synthesis*. New York: Allyn and Bacon, 1970.

[13] W. A. Gardner, *Introduction to Random Processes With Applications to Signals and Systems*, 2nd ed. New York: McGraw Hill, 1989.

[14] C. D. Hull and R. G. Meyer, "A systematic approach to the analysis of noise in mixers," *IEEE Trans. Circuits Syst. I: Fundam. Theory Applicat.*, vol. 40, no. 12, pp. 909–919, Dec. 1993.

[15] H. Darabi and A. A. Abidi, "Noise in RF-CMOS mixers: A simple physical model," *IEEE J. Solid-State Circuits*, vol. 35, no. 1, pp. 15–25, Jan. 2000.

[16] M. T. Terrovitis and R. G. Meyer, "Noise in current-commutating CMOS mixers," *IEEE J. Solid-State Circuits*, vol. 34, no. 6, pp. 772–783, Jun. 1999.

[17] W. A. Garner, *Introduction to Random Processes with Applications to Signals and Systems*, 2nd ed. New York: McGraw-Hill, 1989.

[18] K.-Y. Toh, P.-K. Ko, and R. G. Meyer, "An engineering model for short-channel MOS devices," *IEEE J. Solid-State Circuits*, vol. 23, pp. 950–957, Aug. 1988.

[19] J. Roychowdhury, "Reduced-order modeling of time-varying systems," *IEEE Trans. Circuits Syst. II*, vol. 46, no. 10, pp. 1273–1288, Oct. 1999.

[20] A. Demir, "Analysis and simulation of noise in nonlinear electronic circuits and systems," Ph.D. dissertation, Univ. of California, Berkeley, 1997.

Jongrit Lerdworatawee (S'00–M'05) received the B.S. degree in electrical engineering from Tsinghua University, Beijing, China, in 1998, the M.Eng. degree in electrical engineering from the National University of Singapore, Singapore, in 2000, and the Ph.D. degree in electrical engineering from the University of Southern California, Los Angeles, in 2005.

His research interests are in RF/mixed-signal circuits and signal processing algorithm for data storage systems and wireless communications systems. In 2005, he joined Seagate Research Center, Pittsburgh, PA, as a Research Staff Member developing IC chips for the advanced data storage systems. Since 2006, he has been with the wireless group of Silicon Labs, Austin, TX, where he is involved in the RF/mixed signal IC design for the next-generation single-chip cell phone application.

Won Namgoong received the Ph.D. degree in electrical engineering from Stanford University, Stanford, CA, in 1999.

He is currently with Atheros Communications, Santa Clara, CA, as a Senior Scientist, working on next-generation IC chips for communications. He also serves as a Consulting Associate Professor at Stanford University. His research interests are in signal processing systems, wireless communications, and RF/mixed-signal circuits.

In 2002, Dr. Namgoong received the National Science Foundation (NSF) CAREER Faculty Award while he was an Assistant Professor at the University of Southern California. He has been an Associate Editor for the IEEE TRANSACTIONS ON CIRCUITS AND SYSTEMS, PART I: REGULAR PAPERS, a guest editor for the *Journal of VLSI Signal Processing*, and a member of the ISSCC technical program committee.